

# A Hybrid Knowledge-Guided Detection Technique for Screening of Infectious Pulmonary Tuberculosis from Chest Radiographs

Rui Shen, *Student Member, IEEE*, Irene Cheng, *Senior Member, IEEE*, and Anup Basu, *Senior Member, IEEE*

**Abstract**—Tuberculosis (TB) is a deadly infectious disease and the presence of cavities in the upper lung zones is a strong indicator that the disease has developed into a highly infectious state. Currently, the detection of TB cavities is mainly conducted by clinicians observing chest radiographs. Diagnoses performed by radiologists are labor intensive and very often there is insufficient healthcare personnel available, especially in remote communities. After assessing existing approaches, we propose an automated segmentation technique which takes a hybrid knowledge-based Bayesian classification approach to detect TB cavities automatically. We apply gradient inverse coefficient of variation (GICOV) and circularity measures to classify detected features and confirm true TB cavities. By comparing with non-hybrid approaches and the classical active contour techniques for feature extraction in medical images, experimental results demonstrate that our approach achieves high accuracy with a low false positive rate in detecting TB cavities.

**Index Terms**—Image segmentation, classification, tuberculosis detection, computer-aided detection.

## I. INTRODUCTION

ALTHOUGH effective therapies have reduced the fatality rate from infectious pulmonary tuberculosis (TB), TB continues to be a public health problem of global proportions especially in developing countries [1]. Due to the high infectivity and fatality rate of TB [1], timely detection and treatment is very important. Although cavitation in the lungs is not very common in primary TB, cavitation in the upper lung zones (ULZs, *i.e.*, upper half of a lung) is more common in postprimary TB (also known as typical TB or reactivation TB) and it is an indicator that the disease has developed into a state of high infectivity [2]. Therefore, the detection of such cavitory cases is important in order to prevent further transmission of the disease. In immigration medical examinations, chest radiography is usually used as the primary detection tool for TB [3] [4]. In routine diagnosis of TB, although methods like skin test and blood test can be used, a chest radiograph (CXR) is usually taken when the patient shows pulmonary symptoms [5] or the prevalence of the disease is high in the populations [2]. The combination of radiographic findings and demographic/clinical data helps physicians to decide the possibility of infectious TB. This paper focuses on accurately detecting TB cavities from CXRs. Currently, the detection of TB cavities from CXRs is mainly conducted visually by radiologists based on their knowledge and experience. Examining mass CXRs even

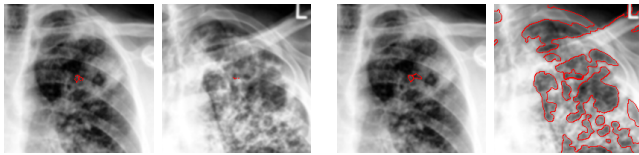
on a periodic basis is too demanding on resources given a limited number of radiologists. The objective of developing computer-aided diagnosis/detection (CAD) system is to make this diagnostic procedure more efficient.

CAD systems dealing with different imaging modalities have been developed for diagnoses of various diseases, and have become commonly used in routine diagnostic procedures, such as the diagnosis of breast cancer and lung cancer [6]. Although numerous techniques for segmenting lung fields have been proposed [7] [8], automatic detection of TB cavities from CXRs has not been adequately studied. Previous researchers have worked on distinguishing abnormal CXRs from normal ones using texture features [9] [10], however, their approaches do not aim to locate cavities. In this paper, we propose a technique to automatically segment and classify TB cavities from digital CXRs. Our method can be applied either independently or as an additional step to previous methods to provide physicians with more information about suspected TB.

Since the presence of cavities in the upper thoracic area often suggests typical TB, automatic segmentation and classification of these cavities taking spatial, geometric and demographic information into consideration is useful for a CAD system. Active contour (AC) models (or snakes) [11] [12] [13] are commonly used as segmentation techniques for medical images, though prior knowledge of the region of interest (ROI) is often needed in order to guide the execution and successful convergence of these algorithms. AC models can be categorized into two types: level set and parametric. The convergence of level set techniques is usually slower than parametric methods because the deformation of a higher dimensional function is required [12]. Besides, level set is very sensitive to noise resulting in the extraction of too many false objects. Given an initial contour, the external and internal forces of parametric snakes drive the evolution and converge to the final contour much faster than level set snakes. However, as discussed in earlier research [13], traditional parametric AC models have limited capture range. It cannot converge accurately unless an initial contour is specified close to the region of interest. Boundary Vector Flow (BVF) [11], an enhanced version of the traditional parametric AC models, has successfully increased the capture range but is not suitable to extract acute concave angles. Since TB cavities are often close to spherical and non-concave, we investigated the feasibility of applying BVF to detect TB cavities. Experimental results show that BVF fails to converge due to complex tissue patterns, *e.g.*, acinar shadows, as shown in Figure 1(a) (only the halves that

R. Shen, I. Cheng and A. Basu are with the Department of Computing Science, University of Alberta, Edmonton, AB, T6G 2E1 Canada. E-mail: {rshen,locheng,basu}@ualberta.ca

contain the cavities are shown). Magnetostatic active contour (MAC) model [12] is a level set snake. Although slower than parametric methods, it is able to extract multiple objects starting from a single initial contour. Since more than one TB cavity is possible in infected lungs, we assess the performance of MAC in segmenting multiple cavities. Test results show that multiple level sets not corresponding to the TB cavities are generated (Figure 1(b)). More test results will be discussed in Section IV. A common weakness of most AC models is the necessity to define an initial contour close to the ROI in order for the algorithms to evolve and converge. Given the large volume of CXRs to be examined, an automatically generated initial contour is desirable.



(a) BVF for single-cavity (left) and two-cavity (right) cases. (b) MAC for single-cavity (left) and two-cavity (right) cases.

Fig. 1. Complex patterns prevent the convergence of BVF in these images. MAC can generate multiple level sets but fail to segment correctly due also to complex patterns.

The major challenge in the cavity detection from CXRs is the complicated texture and varied intensity distribution in the lung fields caused by TB infection (*e.g.*, parenchymal infiltrates and acinar shadows) and the superimposed anatomical structures (*e.g.*, the soft skin, muscles, tissues, organs, and the radiodense ribcage), which may blur the boundaries of the cavities or even partially occlude the cavities. The presence of superimposed anatomical structures makes the discrimination of image features and the interpretation of a CXR extremely challenging even for clinical experts [14]. Various subtraction techniques were discussed in the literature attempting to remove normal or unrelated anatomical structures in CXRs. Dual energy subtraction and temporal subtraction are proposed to characterize abnormal findings especially for subtle lesions. Dual energy subtraction [15] is based on exploiting the differential attenuation of low-energy x-ray photons by calcium to generate separate images for bones and soft tissues. Dual energy subtraction radiography is not fully available for clinical use especially in remote communities. Temporal subtraction [15] [16] based on a previous radiograph of the same patient is not applicable in our case because we are interested in detecting abnormalities in the first CXR of a patient. Without a previous radiograph for comparison, contralateral subtraction [17] [18] assuming the symmetry of the ribcage and the mirroring of the left and right lung fields can be applied. In this case, a possible outcome of this method is the elimination of important features that may appear symmetrically on both sides of the thorax. Another approach is to measure the smoothness across the anatomical structure identifying superimposing borders [19]; or to fit a predefined model to the input image to suppress normal structures [20]. Most of such subtraction approaches are based on the symmetry assumption of the ribcage in

the left and right lungs. However, analysis of the CXRs shows that the conditions, such as the texture and shape, in the individual lungs could vary significantly. Therefore, subtraction techniques cannot be directly applied. To deal with the complicated texture and varied intensity distribution, a clustering and adaptive thresholding scheme coupled with a robust AC model is applied in our approach to extract suspected cavities. True cavities are then distinguished from false positives (FPs) using a Bayesian classifier. Both the segmentation and classification are automatic. We believe that our work is one of the first attempts at automatically locating pulmonary TB cavities in CXRs with high accuracy and low FP rate (FPR).

The rest of the paper is organized as follows. Section II introduces the materials used in this study. Section III explains our proposed technique in detail. Section IV presents experimental results. Section V discusses the limitation of the proposed approach. Finally, conclusion and future work is given in Section VI.

## II. MATERIALS AND PRE-PROCESSING

Two image databases are used in this study. Images are grouped into three sets: 20 in the cavity set, 19 in the non-cavity set, and 110 in the normal set. The images in the cavity set are from patients who were diagnosed with typical TB and showed cavities in CXRs. The images in the non-cavity set are from patients who were diagnosed with typical TB but showed no cavity in CXRs. The images in the normal set are from patients who were not diagnosed with typical TB and showed normal (or close to normal) lungs with no cavity in CXRs. The first database contains 20 posterior-anterior (PA) CXRs with TB cavities, 19 PA CXRs without TB cavities, and 17 PA CXRs of normal cases without evidence of TB collected at hospitals in Alberta, Canada from routine TB diagnosis. All images were read independently by three experienced chest radiologists, who are specialized in TB diagnosis. When the interpretations of an image were different between the radiologists, they re-analyzed the image and came to a consensus. The presence of TB cavities in an image was confirmed by the radiologists. The locations, sizes, and wall thicknesses of the TB cavities in each image were recorded. A cavity is defined as a parenchymal cyst greater than 10mm in diameter. The final diagnoses were made by combining both radiographic and patient-related demographic/clinical information, *e.g.*, age, gender, ethnic group, HIV status, country-of-birth, smear, shortest time-to-culture (days). In the cavity set, 19 CXRs have 1 cavity each and 1 CXR has 2 cavities, which makes 21 cavities in total. Two images in the cavity set are shown in Figure 2. These images usually have low contrast and complicated texture. The complex patterns surrounding a TB cavity are indicated by red arrows. The second database obtained from [21] contains 93 PA CXRs of normal cases. The images were examined by three chest radiologists.

Before applying the proposed technique, every image in the three sets was pre-processed using the following procedure. First, an image is scaled to have pixel size equivalent to 0.7mm with 8-bit intensity. Therefore, a valid cavity should have a

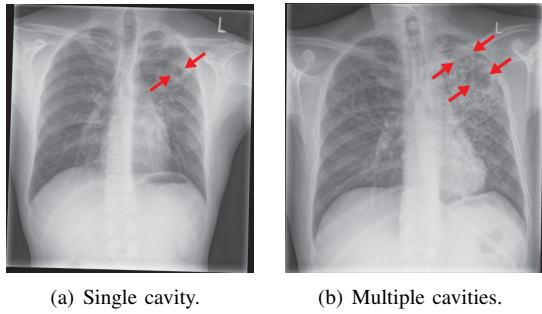


Fig. 2. The original chest radiographs with TB cavities often have low contrast and complicated texture.

diameter greater than 15 pixels. Second, a  $400 \times 200$  window is used to extract the portion of the scaled image that includes most of the ULZs but excludes most of the lower lung zones. The vertical center line of the window is manually aligned with the center line of the spine. Finally, this subimage is histogram equalized and gaussian smoothed to enhance contrast while reducing noise caused by the complicated texture. Figure 3 shows one example of the pre-processed image. The enhanced subimage inside the green rectangle is the result of the pre-processing procedure and it is placed on top of the scaled image to show its relative position. Because of the complicated texture, existing automatic lung segmentation methods [7] [8] tend to extract only part of a lung (*i.e.*, only the darker regions). Therefore, it is difficult to directly apply these methods without adaptation for lungs infected with TB. Instead, after examining 30 pre-processed images, a mask is created to approximate the ULZs, as shown in Figure 4(a). The masked image of the one shown in Figure 3 is displayed in Figure 4(b). Pixels corresponding to the black area in the mask, *i.e.*, pixels outside the ULZs, are discarded when calculating the initial contours and the classification measures.

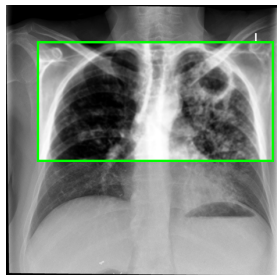


Fig. 3. The pre-processed image. The image in the background is the scaled image. The enhanced subimage inside the green rectangle is the result of the pre-processing procedure.

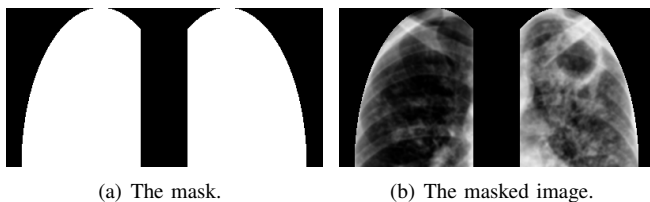


Fig. 4. A mask is used to approximate the ULZs.

### III. A HYBRID KNOWLEDGE-GUIDED DETECTION FRAMEWORK

Differing from many other segmentation methods proposed in the literature, the initialization step in our solution is fully automatic, which is necessary when a large number of CXRs need to be examined. The detection process consists of three phases. In Phase I, adaptive thresholding integrated with an enhanced mean shift technique inspired by [22] is applied to define initial contours of suspected cavities; the initial contours are then converged using an AC model coupled with Dirichlet boundary conditions (BC), following an approach similar to [23]. Our knowledge-guided screening technique eliminates a large proportion of FPs in Phase I, reducing unnecessary computations. In Phase II, the suspected TB cavities are either confirmed or excluded by using optimal thresholds in a Bayesian classification technique based on gradient inverse coefficient of variation (GICOV) [24] and  $M$  circularity measure [25]. If a cavity appears near the clavicles, it is very likely that the cavity is partially occluded (Figure 5), which makes the visible part violate the circularity criterion. In addition, as compared in Figure 5, the radiodense clavicles make the intensity distribution of lung fields near them (inside blue rectangle) quite different from other portions of the lung fields (inside yellow rectangle), which may require a different GICOV threshold. Therefore, if no cavity is confirmed in the clavicular regions in Phase II, those regions go through another segmentation and classification phase (Phase III) using new GICOV and circularity thresholds calculated for them. An overview of the detection framework is given in Figure 6.

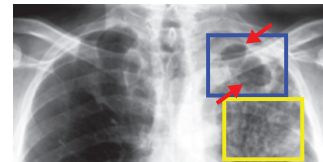


Fig. 5. A cavity is split into two parts by the clavicle. The texture pattern and intensity distribution differ significantly between the region inside the blue rectangle and the region inside the yellow rectangle.

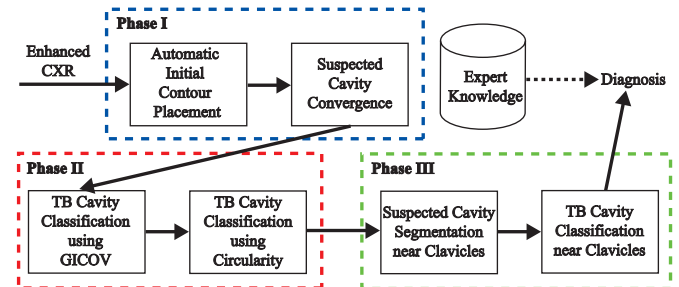


Fig. 6. A hybrid knowledge-guided detection framework.

#### A. Phase I: Automatic Initialization and Convergence of Suspected Cavities

Although AC models based on energy minimization are effective segmentation methods, the traditional AC models

have several drawbacks: they are sensitive to the initial contour placement, can have a capture range too small to detect cavities, may need to apply different parameter values to guide convergence, and do not perform well on weak edges [13]. To deal with these problems and take advantage of the knowledge that the boundaries of TB cavities follow a dark-to-bright transitions in CXRs, we incorporate the directional gradient vector flow (GVF) models combined with Dirichlet BC proposed by Ray and Acton [23] to delineate the suspected TB cavities. This AC model performs well for contrast changes and weak edges. Since multiple cavities can exist (Figure 2(b)), we cannot apply fluid vector flow (FVF) [13], which is designed to segment only a single region.

In contrast to other AC models which require an initial contour to be selected manually, we automate the initial contour placement using mean shift segmentation (Figure 7(b)), and apply adaptive thresholding to control the clustering process. Mean shift [22] is a feature space analysis technique that clusters neighboring data points with similar characteristics using a neighborhood search procedure, which locates the local maxima in a probability density function (PDF), based on the kernel density estimation (or Parzen window method). The mean shift segmentation is based on a recursive mean shift procedure. In this procedure, for each point  $x_i$ , a mean shift vector is defined using the following equation to represent the difference between the weighted mean of a kernel (window)  $G(x)$  and the center  $x$  of the kernel:

$$m_{h,G} = \frac{\sum_{i=1}^n x_i g(\|\frac{x-x_i}{h}\|^2)}{\sum_{i=1}^n g(\|\frac{x-x_i}{h}\|^2)} - x, \quad (1)$$

where  $g(x)$  is the derivative of the selected kernel profile  $k(x)$ , a function used to define the kernel, and  $h$  is the bandwidth that defines the radius of the kernel. Then, the location of  $G$  is shifted by  $m_{h,G}$  until convergence, *i.e.*, the weighted mean of  $G$  and  $x$  overlap. The final location  $y_i$  of  $G$  is given by its center in the last iteration:

$$y_i = \frac{\sum_{i=1}^n x_i g(\|\frac{x-x_i}{h}\|^2)}{\sum_{i=1}^n g(\|\frac{x-x_i}{h}\|^2)}. \quad (2)$$

For image data, each data point (pixel) is treated as a  $d$ -dimensional feature vector that has two components, one spatial component encoded as a 2-dimensional vector (*i.e.*, image coordinates) and one range component encoded as a  $p$ -dimensional vector (*e.g.*, the LUV components for a color image where  $p = 3$ ); and  $d = p + 2$ . Therefore, the kernel is defined to represent the features in both the spatial and range domains:

$$K_{h_s, h_r}(x) = \frac{C}{h_s^2 h_r^p} k(\|\frac{x^s}{h_s}\|^2) k(\|\frac{x^r}{h_r}\|^2), \quad (3)$$

where  $h_s$  and  $h_r$  are the kernel bandwidths in the spatial domain and range domain, respectively;  $x^s$  and  $x^r$  are the spatial and range parts of a feature vector, respectively; and  $C$  is a normalization constant. Now, the bandwidth parameter used in Equation 1 becomes a pair of parameters, *i.e.*,  $\mathbf{h} = (h_s, h_r)$ . As  $h_s$  increases, only large spatial features persist; and as  $h_r$  increases, only features with strong color contrast persist. For

each pixel  $x_i$ , its final value is given by:

$$z_i = (x_i^s, y_{i,c}^r), \quad (4)$$

where  $x_i^s$  denotes the spatial part of the input vector, and  $y_{i,c}^r$  denotes the range part of the kernel location vector at convergence.

After the local maxima are located, the neighboring pixels are clustered towards a local maximum if they are closer than  $h_s$  in the spatial domain and  $h_r$  in the range domain. Finally, spatial regions with less than  $W$  pixels are merged together. The bandwidth parameters and merging parameter are chosen to best segment out the TB cavities in the training image set, which consists of three images. We set  $h = (3, 3)$  and  $W = 50$  so that most pixels inside a TB cavity are grouped into one cluster. As shown in Figure 7(b), the pixels of the single cavity in the right half of the image (left lung) are assigned the same graylevel. Although mean shift was used in many applications, such as image segmentation (described above) and object tracking [26], it has not been used to locate an initial contour as in our solution.

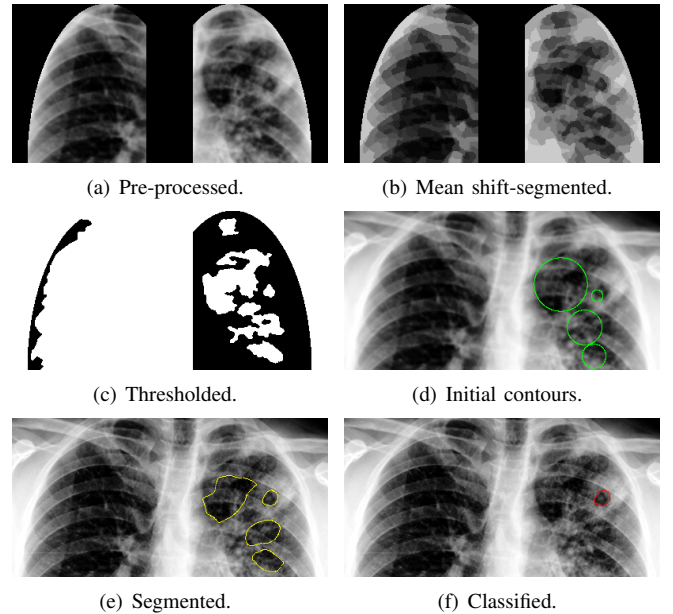


Fig. 7. The original image in Figure 2(a) is pre-processed before the detection procedure.

Selecting a global threshold for the entire image cannot produce accurate result because of the varied intensity distribution. In our adaptive thresholding approach, the threshold needs to be determined by local image attributes which reflect not only the characteristics in the neighborhood, but also the presence of TB cavities if any. In order to discover such an attribute, we perform experiments using the training image set. Due to the destruction of pulmonary tissue caused by TB, the texture of one lung is very likely to be quite different from the other in the same CXR. Therefore, different thresholds should be applied to individual lungs according to their contents. Experimental results suggest that for a lung field  $R_l$ , the threshold  $b$  needed for segmenting out the clusters, which are within a TB cavity, increases as the GICOV threshold  $\gamma$

computed from  $R_l$  increases. This is quite intuitive since the GICOV threshold can be considered as a measure of the level of noise in  $R_l$ . Normally, the higher  $\gamma$  is, the noisier  $R_l$  is. (More description on GICOV will be covered in Sections III-B and III-C). Therefore, the adaptive threshold  $b$  is calculated for each lung field based on  $\gamma$  as:

$$b = a_1\gamma^2 + a_2\gamma + a_3. \quad (5)$$

The coefficients  $a_i$ 's are determined by linear regression using the GICOV thresholds obtained from training images. The binary image after thresholding the mean shift segmented image is shown in Figure 7(c). The combination of the mean shift segmentation and the adaptive thresholding automates the active contour initialization process and saves computational time by excluding a large number of FPs. For each foreground region (white region) inside the ULZs, a circle near the center of the region is chosen as the initial contour for the GVF snake with Dirichlet BC. To accelerate the convergence of the snake, the radius  $R$  of the circle is determined by the size  $S$  of the region:

$$R = \max(3, \sqrt{S/\pi}). \quad (6)$$

The initial contours (green circles) are shown in Figure 7(d). Figure 7(e) shows the segmented suspected TB cavities (yellow contours).

### B. Phase II: Hybrid Knowledge-Guided Classification

After the suspected TB cavities are segmented out from the images, they are classified using a Bayesian classifier. Two features are considered: the inner boundary of a TB cavity usually has dark-to-bright transition; and the shape of a TB cavity often appears circular in a CXR. To best represent the two features, we choose descriptors: the gradient inverse coefficient of variation (GICOV) [24], which is good at describing region boundaries, and the  $M$  circularity measure [25], which is good at describing the circularity of a region. Let  $V$  be the GICOV score and  $M$  be the circularity score obtained from a given contour  $C$ . Let the *a posteriori* probabilities of the class ( $\omega_t$ ) of TB cavities and the class ( $\omega_n$ ) of non-TB cavities given  $V$  be  $P_{\omega_t}(V)$  and  $P_{\omega_n}(V)$  respectively, and given  $M$  be  $P_{\omega_t}(M)$  and  $P_{\omega_n}(M)$  respectively. Then the classification problem can be formulated based on Bayes decision rule:

$$(V, M) \in \begin{cases} \omega_t, & \text{if } (P_{\omega_t}(V) > P_{\omega_n}(V)) \wedge \\ & (P_{\omega_t}(M) > P_{\omega_n}(M)); \\ \omega_n, & \text{otherwise.} \end{cases} \quad (7)$$

Here the thresholds for  $V$  and  $M$  are determined separately instead of using the standard naive Bayes, because  $V$  is employed in the modeling of the PDF of  $M$  (Section III-C). Hence, considering the feature independence assumption in naive Bayes, the current format of the decision rule, *i.e.*, applying the two measures sequentially, is used. After finding the Bayes decision threshold  $\gamma$  for GICOV and  $m$  for circularity such that  $P_{\omega_t}(V) = P_{\omega_n}(V)$  and  $P_{\omega_t}(M) = P_{\omega_n}(M)$ , Equation 7 can be rewritten as:

$$(V, M) \in \begin{cases} \omega_t, & \text{if } (V > \gamma) \wedge (M < m); \\ \omega_n, & \text{otherwise.} \end{cases} \quad (8)$$

Note that the GICOV threshold and circularity threshold are calculated for individual lung fields to accommodate varied image conditions. Using this rule, a true TB cavity can be distinguished from FPs, as marked in red in Figure 7(f). In a practical situation, physicians can combine this rule with expert knowledge about the locations of the cavities and the demographic data of the patient to make the final decision.

The GICOV score  $V$  of a contour is defined as [24]:

$$V = \frac{\bar{X}}{S/\sqrt{n}}, \quad (9)$$

where  $\bar{X}$  is the mean of the directional gradients  $X = \{X_1, \dots, X_n\}$  computed at a set of random sample locations on the contour, and  $S = \text{std}(X)$  is the standard deviation of  $X$ . We assume that  $X$  is computed in 16 cardinal directions, *i.e.*,  $n = 16$ . The direction of the directional gradient  $X_i$  at image location  $(x, y)$  is defined as the unit outward normal  $\vec{n}(x, y)$  at that location, and the magnitude is defined as the sum of the projections of the gradients in the x- and y-directions onto  $\vec{n}(x, y)$ . A higher GICOV score  $V$  of a contour indicates that it resides on a stronger boundary.

The circularity score  $M$  of a contour is defined as [25]:

$$M = \sum_{i=1}^L \frac{\text{var}(d_{i,j})}{\max(d_{i,j})}, \quad (10)$$

where  $L$  is the number of centers of gravity for the contour;  $d_{i,j}$  is the distance from the  $i$ th center of gravity to the contour in the  $j$ th direction ( $j \in \{1, \dots, n\}$ ); and  $\max(d_{i,j})$  serves as a normalization factor to make the measure scale invariant. A perfect circle generates a zero circularity score (*i.e.*,  $M = 0$ ) since  $\text{var}(d_{i,j}) = 0$ . Here we make the following assumptions: 1) each contour has a single center of gravity, *i.e.*,  $L = 1$ ; 2)  $d_{i,j}$  is calculated in 16 cardinal directions, *i.e.*,  $n = 16$ .

### C. Optimal Threshold Selection

The optimal GICOV threshold  $\gamma$  is calculated in a similar way as in [24], which aims to find the critical GICOV score  $\gamma$  such that  $P_{\omega_t}(V) > P_{\omega_n}(V)$  for any  $V > \gamma$ . In order to get the threshold, the GICOV density function needs to be modeled first. We make the following assumption:  $X_i \sim N(\mu_v, \sigma_v^2)$  if  $X_i$  resides on a strong edge; and  $X_i \sim N(0, \sigma_v^2)$  otherwise. The first-order derivative of Gaussian is used to estimate the image gradient,  $g_x(x, y, \sigma_1)$  for the x-direction and  $g_y(x, y, \sigma_1)$  for the y-direction. In [24],  $\mu_v$  and  $\sigma_v$  are estimated using a general noise estimation of the whole image set. This is appropriate only when the gradient intensity distribution has little variation across the whole image set. However, in the case of TB CXRs, the image condition differs significantly even from one region to another in the same image. Therefore, we estimate  $\mu_v$  and  $\sigma_v$  based on the image gradient distribution of each lung field as:

$$\mu_v = \frac{(\max(g_x) - \min(g_x) + \max(g_y) - \min(g_y))/2}{\sqrt{((\text{std}(g_x) + \text{std}(g_y))/2)^2 + 2\pi\sigma_1^2}}, \quad (11)$$

$$\sigma_v = \frac{(\text{std}(g_x) + \text{std}(g_y))/2}{2\sqrt{2\pi\sigma_1^2}}, \quad (12)$$

where we set  $\sigma_1 = 1$  in our experiment. As proved in [24],  $V$  follows a Gaussian distribution  $V \sim N(\frac{\mu_1}{\mu_2}\sqrt{n}, \frac{\sigma_1^2}{\mu_2^2} + \frac{\mu_1^2\sigma_2^2}{\mu_2^4})$ , where  $\mu_1 = r_v\mu_v$ ,  $\sigma_1^2 = \frac{\sigma_v^2}{n}$ ,  $\mu_2 = \frac{\sqrt{\frac{n}{n-1}r_v(1-r_v)\mu_v + \sigma_v^2}}{2\sqrt{\frac{n}{n-1}r_v(1-r_v)\mu_v}}$ , and  $\sigma_2^2 = \frac{\sigma_v^2}{n-1}$ . Here,  $r_v$  is a free parameter representing the percentage of samples that lie on a strong edge. Using Bayes' theorem, the posterior probabilities,  $P_{\omega_t}(V)$  and  $P_{\omega_n}(V)$  used in Equation 7, can be expressed as:

$$P_{\omega_t}(V) = \frac{P(\omega_t)p(V|\omega_t)}{p(V)}, P_{\omega_n}(V) = \frac{P(\omega_n)p(V|\omega_n)}{p(V)}. \quad (13)$$

The goal is to find a threshold  $\gamma$  such that  $P_{\omega_t}(V) = P_{\omega_n}(V)$ , *i.e.*,  $P(\omega_t)p(V|\omega_t) = P(\omega_n)p(V|\omega_n)$ . Same as in [24],  $P(\omega_t)p(V|\omega_t)$  is modeled as the sum of the probabilities of different patterns (*i.e.*, different numbers of sample points lying on a strong edge) belonging to the TB cavity class  $\omega_t$  and  $P(\omega_n)p(V|\omega_n)$  the sum of the probabilities of different patterns belonging to  $\omega_n$ :

$$P(\omega_t)p(V|\omega_t) = \sum_{j=r_v n}^n \pi_j p(V|j), \quad (14)$$

$$P(\omega_n)p(V|\omega_n) = \sum_{j=0}^{r_v n-1} \pi_j p(V|j), \quad (15)$$

where  $\pi_j = C_n^j p_v^j (1-p_v)^{n-j}$  represents the prior probability of pattern  $j$ , which is assumed to follow a binomial distribution. This means that a contour with at least  $r_v n$  samples lying on strong edges satisfies the GICOV measure.

The optimal circularity threshold is computed in a similar fashion, which aims to find the critical circularity score  $m$  such that  $P_{\omega_t}(M) > P_{\omega_n}(M)$  for any  $M < m$ . In order to model the circularity density function, we make the following assumption:  $d_{i,j} \sim N(0, \sigma_m^2)$  if the sample in the  $j$ th direction resides on a perfect circle; and  $d_{i,j} \sim N(\mu_m, \sigma_m^2)$  otherwise. In our experiment, we find that a region in a CXR with higher level of noise ( $\mu_v$  and  $\sigma_v$  are large) usually generates higher GICOV threshold. Therefore, the GICOV threshold  $\gamma$  of a region can serve as a measure of the noise level in that region. It is more difficult to perceive a perfect circle in a noisier region in a CXR. Therefore, higher  $\gamma$  indicates lower chance of observing low  $m$ . Based on this observation,  $\mu_m$  and  $\sigma_m$  are estimated as functions of  $\gamma$ . Through experiments on the training set, we found the following forms of  $\mu_m$  and  $\sigma_m$  give the best discrimination between  $P_{\omega_t}(M)$  and  $P_{\omega_n}(M)$ :

$$\mu_m = \log_{\pi} \gamma, \quad (16)$$

$$\sigma_m = (\log_{\pi} \gamma)^2. \quad (17)$$

$\max(d_{i,j})$  is estimated by solving  $Pr(d_{i,j} \leq \max(d_{i,j})) \geq c_m$ , which gives the following solution according to the connection between probability theory and theory of errors [27]:

$$\max(d_{i,j}) \geq \mu_m + \sqrt{2}\sigma_m \text{erf}^{-1}(2c_m - 1), \quad (18)$$

where  $\text{erf}^{-1}(\cdot)$  is the inverse Gaussian error function. Equation 18 gives a lower bound of  $\max(d_{i,j})$ . In our experiment, we use the following equation to estimate  $\max(d_{i,j})$ :

$$\max(d_{i,j}) = 8(\mu_m + \sqrt{2}\sigma_m \text{erf}^{-1}(2c_m - 1)). \quad (19)$$

Like  $S$  in Equation 9, which is proved to follow a Gaussian distribution [24],  $M$  also follows a Gaussian distribution  $M \sim N(\mu_3, \sigma_3^2)$ , where  $\mu_3 = \frac{\sqrt{\frac{n}{n-1}r_m(1-r_m)\mu_m + \sigma_m^2}}{2\sqrt{\frac{n}{n-1}r_m(1-r_m)\mu_m} \max(d_{i,j})}$  and  $\sigma_3^2 = \frac{\sigma_m^2}{(n-1)\max(d_{i,j})^2}$ . Similar to the GICOV threshold selection,  $P_{\omega_t}(M)$  and  $P_{\omega_n}(M)$  can be decomposed using Bayes' theorem, and  $P(\omega_t)p(M|\omega_t)$  and  $P(\omega_n)p(M|\omega_n)$  are modeled as:

$$P(\omega_t)p(M|\omega_t) = \sum_{j=0}^{r_m n-1} \pi_j p(M|j), \quad (20)$$

$$P(\omega_n)p(M|\omega_n) = \sum_{j=r_m n}^n \pi_j p(M|j), \quad (21)$$

where  $\pi_j = C_n^j p_m^j (1-p_m)^{n-j}$  represents the prior probability of pattern  $j$ , which is assumed to follow a binomial distribution. This means that a contour with at least  $(1-r_m)n$  samples lying on a perfect circle satisfies the circularity measure. Note that the GICOV threshold  $\gamma$  and the circularity threshold  $m$  are calculated for every single lung field, since the conditions of the image regions (*e.g.*, texture and contrast) vary significantly.

#### D. Phase III: Cavity Detection in the Clavicular Regions

If no cavity is detected in regions near clavicles, this third phase is performed to detect cavities in those regions, which may be missed by the previous two phases due to the radiodense clavicles. The upper half of the ULZs extracted by the mask (Figure 4(a)) is considered as the clavicular regions. The GICOV thresholds  $\gamma'$  are calculated using the same procedure in Section III-C but only based on pixels in the clavicular regions. Since cavities detected in these regions usually do not satisfy the circularity criterion due to occlusion by the clavicles, a higher circularity threshold  $m' = 3m$  is used, where  $m$  is the threshold calculated for that whole ULZ.

## IV. EXPERIMENTAL RESULTS AND ANALYSIS

The goal of our experiments is to verify the effectiveness of the detection framework using the proposed classification measures, *i.e.*, GICOV alone, circularity alone, and the hybrid approach, in identifying TB cavities.

#### A. Experiment I - Verifying the Proposed Detection Technique

In the first set of tests, the proposed hybrid technique is evaluated using all the images in the three image sets. 4 images in the cavity set (one cavity in each image), 4 images in the non-cavity set and 10 images in the normal set serve as the training set, while all the other 131 images are used as the test set. Figure 8 shows the Bayes decision rules for 2 cavitory cases in the training set derived from PDFs. The charts in the first row illustrate the Bayes decision rules given GICOV scores for the ULZs that contain TB cavities. The vertical axis represents the probability, and the horizontal axis represents the GICOV score. The blue curves are the PDFs for  $P(\omega_t)p(V|\omega_t)$  and the red curves are the PDFs for  $P(\omega_n)p(V|\omega_n)$ . The charts in the second row illustrate the Bayes decision rules given GICOV scores for clavicular

TABLE I

DETECTION RESULTS ON THE TRAINING AND TEST SETS. FOR THE TEST SET, THE TPR IS 82%, WHILE THE FPR IS 0.9/IMAGE ON THE CAVITY SET, 0.7/IMAGE ON THE NON-CAVITY SET, AND ONLY 0.05/IMAGE ON THE NORMAL SET.

	Training Set				Test Set			
	C Set	NC Set	N Set	All	C Set	NC Set	N Set	All
# of Images	4	4	10	18	16	15	100	131
# of Cavities	4	0	0	4	17	0	0	17
# of TP	4	—	—	4	14	—	—	14
TPR (%)	100	—	—	100	82.35	—	—	82.35
# of FP	3	2	0	5	15	11	5	31
FPR (#/image)	0.75	0.5	0	0.278	0.938	0.733	0.05	0.237
# of Missing	0	—	—	0	3	—	—	3
Average Time (sec/image)	26.415	7.798	4.446	10.073	34.981	19.868	3.217	8.469

C Set: cavity set; NC Set: non-cavity set; N Set: normal set.

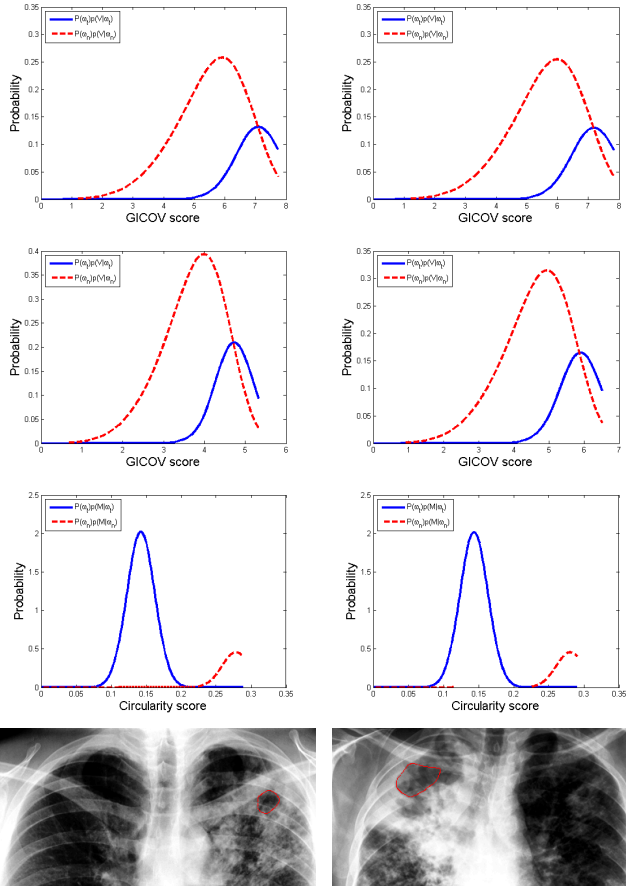


Fig. 8. The Bayes decision rules given GICOV scores for the cavity ULZs (first row), the Bayes decision rules given GICOV scores for the clavicular regions in the cavity ULZs (second row), the Bayes decision rules given circularity scores for right lungs (third row), and the detection results (last row) using both GICOV and circularity measures for the training images.

regions in the cavity ULZs. The charts in the third row illustrate the Bayes decision rules given circularity scores for the ULZs. The vertical axis represents the probability, and the horizontal axis represents the circularity score. The blue curves are the PDFs for  $P(\omega_t)p(M|\omega_t)$  and the red curves are the PDFs for  $P(\omega_n)p(M|\omega_n)$ . The last row displays the detection results using both GICOV and circularity measures. Red contours are TPs. The optimal thresholds for the training set were obtained by using the following parameters:  $r_v = 70\%$ ,  $p_v = 57\%$ ,  $r_m = 60\%$ ,  $p_m = 70\%$ , and  $c_m = 85\%$ . Different

values of the parameters were tested, and the thresholds determined by this set of parameters produced the highest precision (*i.e.*, # of TP/(# of TP + # of FP)) when the highest TP rate (TPR) was achieved on the training set. Therefore, this set of parameters was applied to the test set. The result of the linear regression for calculating the coefficients of the adaptive thresholding in Equation 5 is depicted in Figure 9. The horizontal axis represents the GICOV score and the vertical axis represents the threshold value. The resulting coefficients are:  $a_1 = 10.977$ ,  $a_2 = -118.784$ , and  $a_3 = 389.359$ . For the two cases in Figure 8, the optimal GICOV thresholds  $\gamma$  for the cavity ULZs are 7.137 and 7.229, and the optimal GICOV thresholds  $\gamma'$  for the clavicular regions in the cavity ULZs are 4.729 and 5.905. The optimal circularity thresholds  $m$  for the cavity ULZs are 0.223 and 0.225, and the optimal circularity thresholds  $m'$  for the clavicular regions in the cavity ULZs are 0.669 and 0.675.

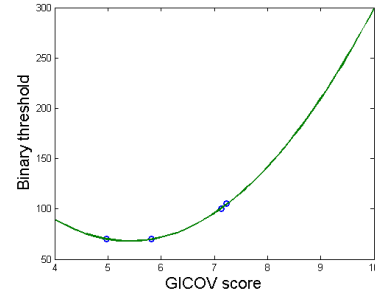


Fig. 9. The adaptive threshold. The horizontal axis represents the GICOV score and the vertical axis represents the threshold value. The resulting coefficients are:  $a_1 = 10.977$ ,  $a_2 = -118.784$ , and  $a_3 = 389.359$ .

The performance of our detection method taking both GICOV and circularity scores into consideration is shown in Figure 10 as an FROC (free response operator characteristics) [28] curve for the test set (131 images). The TPR is measured as a function of the FPR. Higher TPR is achieved at the cost of higher FPR. However, even at the highest TPR that is achieved, the average FPR can be as low as 0.237/image. The detection results at average FPR equivalent to 0.237/image (red cross in Figure 10), as well as the performance on the training set, are summarized in Table I. The detection accuracy on the training set (18 images) is 100% with 5 FPs but no missing TP. The detection accuracy on the test set is 82.35% with 31 FPs and 3 missing TPs. Most FPs are generated in the cavity set and the

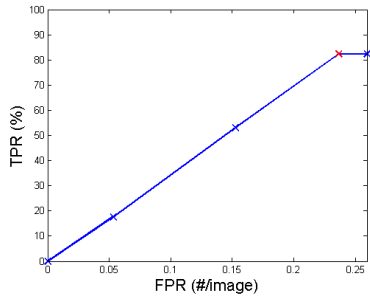


Fig. 10. FROC curve of our detection method for the test set. Higher TPR is achieved at the cost of higher FPR. However, even at the highest TPR that is achieved, the average FPR can be as low as 0.237/image.

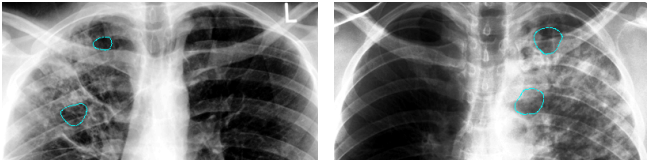


Fig. 11. Complicated texture in typical cases tends to trigger FPs (the cyan contours).

non-cavity set, both of which are CXRs of typical TB cases. These typical cases usually show abnormal texture patterns in the lung fields, which makes them prone to trigger FPs. Two such cases from the non-cavity set are shown in Figure 11. The cyan contours are FPs. In contrast, the FPRs are no higher than 0.05/image for both the normal training set and the normal test set, and less than 0.3/image for both the entire training set and the entire test set.

The entire algorithm was implemented in Matlab and was run on a 2.53GHz dual-core laptop with 4GB memory. Depending on the complexity of the texture, the computational times for the images vary. The average computational times for different image sets are reported in Table I. The cavity set has the highest average processing time, while the normal set has the lowest. The most time consuming part in our algorithm is using an AC algorithm to segment out suspected TB cavities. The computational complexity is roughly proportional to the number of suspected TB cavities that are delineated by the AC algorithm.

### B. Experiment II - Comparing the Three Proposed Classification Measures

In the second set of tests, the performance of the three proposed classification techniques: GICOV alone, circularity alone, and hybrid, are compared. The whole test set in the previous experiment was used and the results are reported in Table II. All the three classification methods follow the same segmentation procedure. The hybrid approach demonstrates the best overall performance among the three with the FPR as 0.237/image for all the 131 test CXRs and 0.05/image for the 100 normal test CXRs, while the rate is almost doubled when using GICOV alone or circularity alone. The comparison of two test images using different classification measures are illustrated in Figure 12. For the image on the left, using GICOV alone produces 2 FPs, while the other two methods



(a) GICOV alone.



(b) Circularity alone.

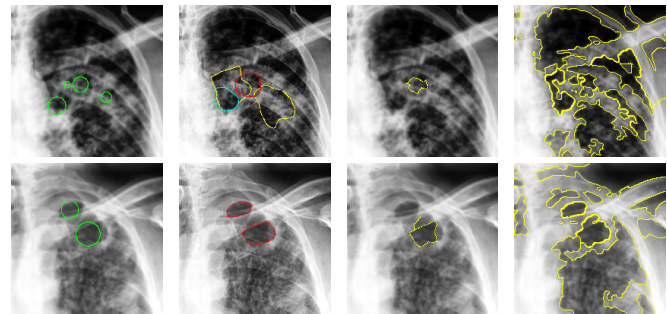


(c) Hybrid.

Fig. 12. Comparison of performance using different proposed classification measures on two test images. Using the hybrid classification method produces fewer FPs than using GICOV alone or using circularity alone.

generate only 1 FP each. For the image on the right, using the hybrid classification method produces 1 FP, while the other two produces 3 and 2 FPs respectively.

### C. Experiment III - Integrating Our Automatic Initialization into BVF and MAC, and Comparing the Results with Our Technique



(a) Initialization. (b) Proposed. (c) BVF. (d) MAC.

Fig. 13. Comparison of our technique with BVF and MAC using our automatic initialization technique. Only the half ULZs that contain cavities are shown. In our results, TPs are indicated in red, FPs in cyan, and other delineated contours in yellow. The contours converged using BVF or MAC are indicated in yellow. All the initial contours (green circles) are generated automatically using our method. Our algorithm can delineate the cavity boundaries very well, while BVF fails to deal with such noisy images and MAC fails to successfully identify all the boundaries.

As reviewed in Section I, active contour models discussed in the literature require the initial contour to be specified. Providing a precise initial contour on every image is impossible when there is a big volume of CXRs to be examined. In CAD, a reasonable approach is to approximate a location in the lung field and start the snake evolution. We first tested a simple automatic initialization scheme by choosing the mid-point in

TABLE II

COMPARISON OF THE PERFORMANCE USING DIFFERENT CLASSIFICATION MEASURES ON THE TEST SET. THE HYBRID APPROACH DEMONSTRATES THE BEST OVERALL PERFORMANCE AMONG THE THREE WITH THE FP RATE AS 0.237/IMAGE FOR ALL THE 131 TEST CXRS AND 0.05/IMAGE FOR THE 100 NORMAL TEST CXRS, WHILE THE RATE IS ALMOST DOUBLED WHEN USING GICOV ALONE OR CIRCULARITY ALONE.

Measures	C Set				NC Set		N Set		All	
	# of TP	TPR	# of FP	FPR	# of FP	FPR	# of FP	FPR	TPR	FPR
GICOV	14	82.35%	33	2.063/image	17	1.133/image	7	0.07/image	82.35%	0.435/image
Circularity	14	82.35%	36	2.25/image	14	0.933/image	5	0.05/image	82.35%	0.420/image
Hybrid	14	82.35%	15	0.938/image	11	0.733/image	5	0.05/image	82.35%	0.237/image

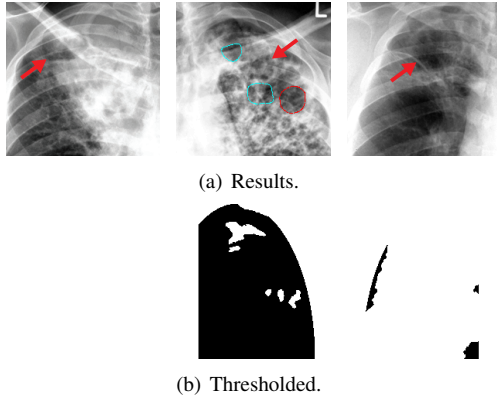


Fig. 14. Three cavities are missed by our technique because automatic initialization fails to place initial contours inside the cavities.

each image, which is roughly in the middle of the ULZ, to initialize a circle with a radius of three pixels as an initial snake. 10 CXRs from the cavity set and another 10 CXRs from the normal set are used to assess the feasibility of applying this simple automatic initialization to BVF and MAC. Incorrect convergences are reported in both cases, and neither BVF nor MAC is able to segment the TB cavities correctly.

By introducing an adaptive thresholding approach, our TB cavity detection technique is able to perform initialization automatically. In order to compare the convergence capability, we provide the initial contours to execute BVF and MAC on 10 cavity cases. The segmentation results using our algorithm on two test images are compared with those generated by BVF and MAC in Figure 13. Only the half ULZs that contain cavities are shown. In the results using our technique, TPs are indicated in red, FPs in cyan, and other delineated contours in yellow. The contours converged to using BVF or MAC are indicated in yellow. All the initial contours (green circles) in this comparison are generated automatically using our method. Since BVF cannot segment multiple regions, only images with single TB cavities are used and only those initial contours within a confirmed TB cavity are used as initial snakes. If a cavity is split into two parts by the clavicle, only the initial contour in the larger part is used. For our technique and MAC, all the initial contours are used. Our algorithm can delineate the cavity boundaries very well, while BVF fails to deal with such noisy images and MAC fails to successfully identify all the boundaries.

## V. LIMITATION

Figure 14(a) (only the cavity ULZs are displayed) shows the three cavities (indicated by red arrows) missed by our

method. This problem arises because automatic initialization fails to place initial contours inside the cavities, as shown in Figure 14(b). For computational efficiency, we use GICOV to measure the texture complexity in our current thresholding scheme. Since the adaptive threshold is determined based on the pixels in the whole ULZ including background, it may fail when the intensity distribution varies significantly from one portion of the image to another, especially when the boundary of the cavity is weak. To address the missing cavity issue, we will explore the possibility of incorporating other techniques in the future, such as locally adaptive thresholding or a template-based scheme.

## VI. CONCLUSION AND FUTURE WORK

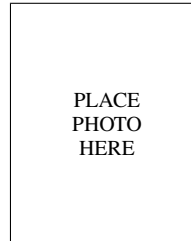
In this paper, we proposed a novel hybrid approach for automatic TB cavity detection from chest radiographs. To the best of our knowledge, no automatic algorithm has been developed that can detect TB cavities from CXRs accurately. Our approach first applies an enhanced mean shift segmentation technique integrated with adaptive thresholding to automate the initial contour placement. These initial contours are used in a GVF snake model with Dirichlet boundary conditions to segment out suspected features. In the subsequent Bayesian classification process, GICOV and circularity thresholds are applied. Experimental results demonstrate that our method achieves good accuracy with a low FPR, *i.e.*, 82.35% TPR and 0.237 FP per image on the 131 test CXRs, which outperforms using the GICOV indicator alone or the circularity score alone. For CXRs of normal lungs, the FPR is as low as 0.05/image. We also compared our results with those generated by BVF and MAC, and find that other active contour models are not able to segment TB cavities in the test CXRs due to the complex tissue patterns. Given a shortage of radiologists on site, our technique can be used to eliminate a large number of normal and suspected cases so that physicians can focus on a smaller set of patients. Our contribution also lies in introducing automatic initialization which is important for CAD systems. In future work, we will look into an automatic lung field segmentation technique, which may optimize the adaptive thresholding process and improve the accuracy of initial contour placement. We will also explore the possibility of employing other classifiers and features. In addition, we will explore techniques to approximate the geometric attributes of TB cavities such as wall thickness, in order to provide more detailed analysis for infectious pulmonary TB diagnosis.

## ACKNOWLEDGMENT

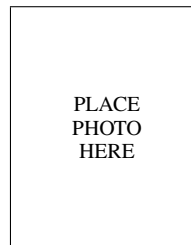
The authors thank Dr. Richard Long, TB Research Center, and Dr. Nilanjan Ray, University of Alberta, for providing the TB image dataset, and for helpful discussions. The authors also thank Kwok Wing Sum and Paul Cheung, University of Hong Kong, for providing their code of BVF. Thanks also go to Xianghua Xie, University of Wales, and Majid Mirmehdi, University of Bristol, for providing their program of MAC. The support of Killam Trusts, iCORE, and Alberta Advanced Education and Technology is gratefully acknowledged.

## REFERENCES

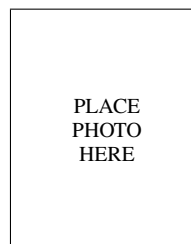
- [1] World Health Organization, "Epidemiology," in *Global Tuberculosis Control: Epidemiology, Strategy, Financing*. WHO Press, 2009, pp. 6–33.
- [2] L. Curvo-Semedo, L. Teixeira, and F. Caseiro-Alves, "Tuberculosis of the chest," *European Journal of Radiology*, vol. 55, no. 2, pp. 158–172, 2005.
- [3] K. P. Cain, S. R. Benoit, C. A. Winston, and W. R. Mac Kenzie, "Tuberculosis among foreign-born persons in the United States," *Journal of the American Medical Association*, vol. 300, no. 4, pp. 405–412, 2008.
- [4] E. Klinkenberg, D. Manissero, J. C. Semenza, and S. Verver, "Migrant tuberculosis screening in the EU/EFTA: yield, coverage and limitations," *European Respiratory Journal*, vol. 34, no. 5, pp. 1180–1189, 2009.
- [5] P. C. Hopewell, M. Pai, D. Maher, M. Uplekar, and M. C. Raviglione, "International standards for tuberculosis care," *The Lancet Infectious Diseases*, vol. 6, no. 11, pp. 710–725, 2006.
- [6] K. Doi, "Computer-aided diagnosis in medical imaging: historical review, current status and future potential," *Computerized Medical Imaging and Graphics*, vol. 31, no. 4–5, pp. 198–211, 2007.
- [7] A. Myronenko and X. Song, "Global active contour-based image segmentation via probability alignment," in *CVPR*, 2009.
- [8] B. van Ginneken and B. ter Haar Romeny, "Automatic segmentation of lung fields in chest radiographs," *Medical Physics*, vol. 27, no. 10, pp. 2445–2455, 2000.
- [9] Y. Arzhaeva, M. Prokop, D. Tax, P. De Jong, C. Schaefer-Prokop, and B. van Ginneken, "Computer-aided detection of interstitial abnormalities in chest radiographs using a reference standard based on computed tomography," *Medical Physics*, vol. 34, no. 12, pp. 4798–4809, 2007.
- [10] B. van Ginneken, S. Katsuragawa, B. ter Haar Romeny, K. Doi, and M. Viergever, "Automatic detection of abnormalities in chest radiographs using local texture analysis," *IEEE Transactions on Medical Imaging*, vol. 21, no. 2, pp. 139–149, 2002.
- [11] K. Sum and P. Cheung, "Boundary vector field for parametric active contours," *Pattern Recognition*, vol. 40, no. 6, pp. 1635–1645, 2007.
- [12] X. Xie and M. Mirmehdi, "MAC: Magnetostatic active contour model," *IEEE Transactions on Pattern Analysis and Machine Intelligence*, vol. 30, no. 4, pp. 632–645, 2008.
- [13] T. Wang, I. Cheng, and A. Basu, "Fluid vector flow and applications in brain tumor segmentation," *IEEE Transactions on BioMedical Engineering*, vol. 56, no. 3, 2009, 781–789.
- [14] B. van Ginneken, B. ter Haar Romeny, and M. Viergever, "Computer-aided diagnosis in chest radiography: a survey," *IEEE Transactions on Medical Imaging*, vol. 20, no. 12, pp. 1228–1241, 2001.
- [15] H. MacMahon, F. Feng, R. Engelmann, R. Roberts, and S. Armato, "Dual energy subtraction and temporal subtraction chest radiography," *Journal of Thoracic Imaging*, vol. 23, no. 2, pp. 77–85, 2008.
- [16] H. Zhao, S.-C. B. Lo, M. T. Freedman, and S. K. Mun, "Automatic temporal subtraction of chest radiographs and its enhancement for lung cancers," in *Proceedings of SPIE*, vol. 4322, 2001, pp. 1867–1872.
- [17] Q. Li, S. Katsuragawa, T. Ishida, H. Yoshida, S. Tsukuda, H. MacMahon, and K. Doi, "Contralateral subtraction: A novel technique for detection of asymmetric abnormalities on digital chest radiographs," *Medical Physics*, vol. 27, no. 1, pp. 47–55, 2000.
- [18] S. Tsukuda, A. Heshiki, S. Katsuragawa, Q. Li, H. MacMahon, and K. Doi, "Detection of lung nodules on digital chest radiographs: Potential usefulness of a new contralateral subtraction technique," *Radiology*, vol. 223, no. 1, pp. 199–203, April 2002.
- [19] H. Yoshida and K. Doi, "Computerized detection of pulmonary nodules in chest radiographs: Reduction of false positives based on symmetry between left and right lungs," in *Proceedings of SPIE*, vol. 3979, 2000, pp. 97–102.
- [20] F. Vogelsang, M. Kohnen, H. Schneider, F. Weiler, M. Kilbinger, B. Wein, and R. Guenther, "Skeletal maturity determination from hand radiograph by model based analysis," in *Proceedings of SPIE*, vol. 3979, 2000, pp. 294–305.
- [21] J. Shiraishi, S. Katsuragawa, J. Ikezoe, T. Matsumoto, T. Kobayashi, K. Komatsu, M. Matsui, H. Fujita, Y. Kodera, and K. Doi, "Development of a digital image database for chest radiographs with and without a lung nodule: Receiver operating characteristic analysis of radiologists' detection of pulmonary nodules," *American Journal of Roentgenology*, vol. 174, no. 1, pp. 71–74, 2000.
- [22] D. Comaniciu and P. Meer, "Mean shift: a robust approach toward feature space analysis," *IEEE Transactions on Pattern Analysis and Machine Intelligence*, vol. 24, no. 5, pp. 603–619, 2002.
- [23] N. Ray and S. Acton, "Active contours for cell tracking," in *SSIAI*, 2002, pp. 274–278.
- [24] G. Dong, N. Ray, and S. Acton, "Intravital leukocyte detection using the gradient inverse coefficient of variation," *IEEE Transactions on Medical Imaging*, vol. 24, no. 7, pp. 910–924, 2005.
- [25] C. Di Ruberto and A. Dempster, "Circularity measures based on mathematical morphology," *Electronics Letters*, vol. 36, no. 20, pp. 1691–1693, 2000.
- [26] D. Comaniciu, V. Ramesh, and P. Meer, "Real-time tracking of non-rigid objects using mean shift," in *CVPR*, vol. 2, 2000, pp. 142–149.
- [27] G. Marsaglia, "Evaluating the normal distribution," *Journal of Statistical Software*, vol. 11, no. 4, 2004.
- [28] P. C. Bunch, J. F. Hamilton, G. K. Sanderson, and A. H. Simmons, "A free-response approach to the measurement and characterization of radiographic-observer performance," *Journal of Applied Photographic Engineering*, vol. 4, no. 4, pp. 166–171, 1978.



**Rui Shen** Biography text here.



**Irene Cheng** Biography text here.



**Anup Basu** Biography text here.